MARINE GEOPHYSICS

New global marine gravity model from CryoSat-2 and Jason-1 reveals buried tectonic structure

David T. Sandwell,[1]* R. Dietmar Müller,[2] Walter H. F. Smith,[3] Emmanuel Garcia,[1] Richard Francis[4]

Gravity models are powerful tools for mapping tectonic structures, especially in the deep ocean basins where the topography remains unmapped by ships or is buried by thick sediment. We combined new radar altimeter measurements from satellites CryoSat-2 and Jason-1 with existing data to construct a global marine gravity model that is two times more accurate than previous models. We found an extinct spreading ridge in the Gulf of Mexico, a major propagating rift in the South Atlantic Ocean, abyssal hill fabric on slow-spreading ridges, and thousands of previously uncharted seamounts. These discoveries allow us to understand regional tectonic processes and highlight the importance of satellite-derived gravity models as one of the primary tools for the investigation of remote ocean basins.

Fracture zones (FZs) spanning the ocean basins reveal the breakup of the continents and the geometry of sea-floor spreading (1). The exact intersection points of the FZs along conjugate continental margins are used for precise reconstruction of the continents (2–4). These FZ intersections are commonly buried by several kilometers of sediments that flow off the continents to fill the voids created by the thermal subsidence of the rifted margins (5). This sediment cover extends hundreds to

[1]Scripps Institution of Oceanography, La Jolla, CA 92093, USA. [2]EarthByte Group, School of Geosciences, University of Sydney, New South Wales, Australia. [3]Laboratory for Satellite Altimetry, National Oceanic and Atmospheric Administration (NOAA), College Park, MD 20740, USA. [4]European Space Agency/European Space Research and Technology Centre, Keplerlaan 1, 2201AZ Noordwijk, Netherlands.
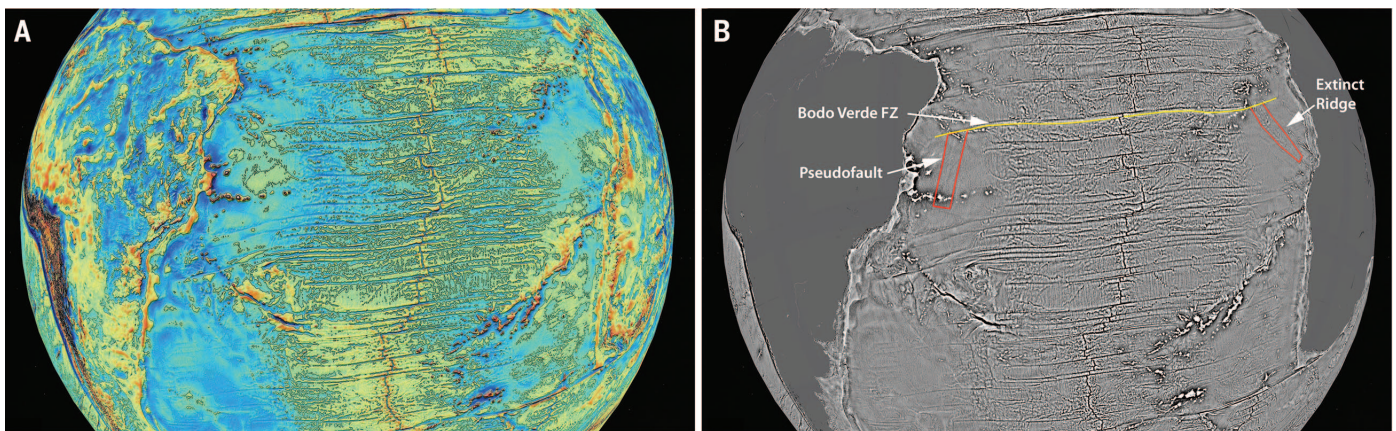*Corresponding author. E-mail: dsandwell@ucsd.edu

thousands of kilometers out onto the oceanic lithosphere, resulting in a relatively flat and featureless sea floor. Reflection seismic profiles can reveal the underlying basement topography of the FZs, but the data coverage is usually insufficient to map out the intersections. In areas of thin sediment cover, the topographic ridges and troughs along the FZs produce large gravity anomalies that are easily traced across the ocean basins (Fig. 1). However, when the topography becomes buried by sediment, the original density contrast of the sea-floor topography is reduced, resulting in more-subdued, and sometimes sign-reversed, gravity signatures (6). Moreover, as the lithosphere ages and cools, the sea floor subsides, causing a blurring of the gravity anomalies; smaller wavelengths of the gravity field become less well-resolved with increasing water depth. Previous global marine gravity models derived from satel-

lite altimetry had sufficient accuracy and coverage to map all FZs in unsedimented sea floor (7), but the 3 to 5 mGal of gravity noise blurred the small signatures of sediment-covered topography such as seamounts and FZs. Here we report on a new global marine gravity model having ~2-mGal accuracy that is providing a dramatically improved resolution of the 80% of the sea floor that remains uncharted or is buried beneath thick sediment.

Gravity-field accuracy derived from satellite altimetry depends on three factors: altimeter range precision, spatial track density, and diverse track orientation. Two altimeter data sets with high track density have recently become available (CryoSat-2 and Jason-1) to augment the older altimeter data (Geosat and ERS-1), resulting in improvement by a factor 2 to 4 in the global marine gravity field. Their newer radar technology results in a 1.25-times improvement in range precision that maps directly into gravity-field improvement (8). The new altimeters also contribute more than 70 months of data, as compared with the 31 months provided by the older satellites. CryoSat-2 has provided the most dense track coverage, because although it has a nominal 369-day repeat orbit period, the ground tracks are allowed to drift within a 5-km band, so after 4 years in orbit it has provided a nominal track spacing of about 2.5 km. Jason-1 provided 14 months of dense track coverage during its geodetic phase, resulting in a track spacing of 7.5 km.

Most of the improvement in the altimeter-derived gravity field occurs in the 12- to 40-km wavelength band, which is of interest for the investigation of structures as small as 6 km. The current version of the altimeter-derived gravity field has an accuracy of about 2 mGal (8). Unlike terrestrial gravity, where coverage is uneven, these accuracies are available over all marine areas and large inland bodies of water, so this gravity provides an important tool for exploring the deep ocean basins. At scales smaller than 200 km, variations in marine gravity primarily reflect

Fig. 1. Ocean gravity maps. (**A**) New marine gravity anomaly map derived from satellite altimetry reveals tectonic structures of the ocean basins in unprecedented detail, especially in areas covered by thick sediments. Land areas show gravity anomalies from Earth Gravitational Model 2008 (15). (**B**) VGG map derived from satellite altimetry highlights FZs crossing the South Atlantic Ocean basin (yellow line). Areas outlined in red are small-amplitude anomalies in areas where thick sediment has diminished the gravity signal of the basement topography. The full-resolution gravity anomaly and VGG models can be viewed in Google Earth using the following files: ftp://topex.ucsd.edu/pub/global_grav_1min/global_grav.kmz and ftp://topex.ucsd.edu/pub/global_grav_1min/global_grav_gradient.kmz. The grids are available in the supplementary material, as well as at the following FTP site: ftp://topex.ucsd.edu/pub/global_grav_1min.
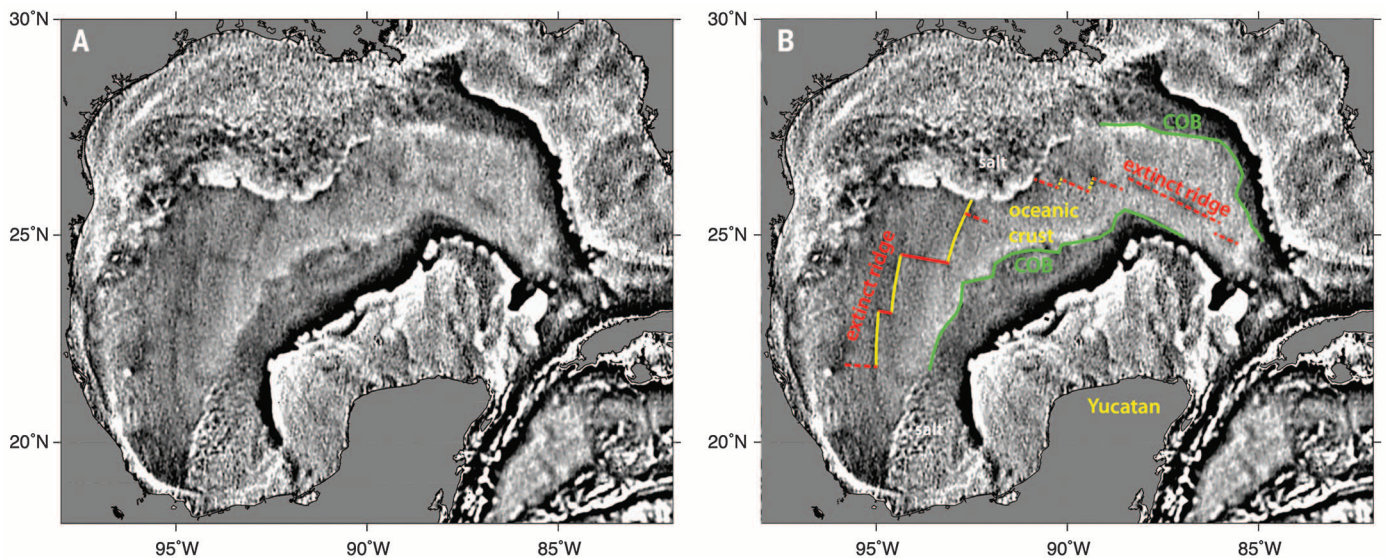
Fig. 2. Gulf of Mexico VGG. (**A**) Uninterpreted. (**B**) Our interpretation of tectonic structures, after Pindell and Kennan (9). The VGG reveals subtle signatures of the extinct spreading ridges and FZs as well as a significant change in amplitude across the boundary between continental and oceanic crust (COBs). This is a Mercator projection; grayscale saturates at ±20 eotvos units.

sea-floor topography generated by plate tectonics such as ridges, FZs, and abyssal hills. Many FZs can now be traced much more closely to the continental margins, and one can also better interpret buried, migrating, unstable FZs, which has the potential to improve the use of FZs as tie points for reconstructions of the boundaries between continental fit reconstructions (Fig. 1). In addition to FZs, there are other tectonic features associated with continental margins, such as the boundaries between continental and oceanic crust [continent-ocean boundaries (COBs)], that can now be mapped in greater detail.

The first example (Fig. 2) is in the Gulf of Mexico, where thick sediments obscure the FZs and extinct ridges. Reconstruction models provide the overall framework of counterclockwise rotation of the Yucatan plate with respect to North America, as well as a generalized position for the COB (9). The new vertical gravity gradient images confirm and refine the positions of these tectonic boundaries. Extinct spreading ridges produce a negative gravity signature, because the relatively high-density sediment cover largely cancels the positive gravity effect of the topographic ridge, leaving the negative gravity signature of the compensating Moho topography (6). In this region, the Moho is more than 15 km beneath the sea surface, so the effects of upward continuation reduce and smooth the anomaly.

The second example is on the African ridge flank, where the new data reveal a major tectonic feature that was not visible in previous satellite gravity data sets because of high-frequency noise. The newly discovered feature is a set of tectonic lineaments roughly between 8°S and 12°S, striking northwest-southeast and obliquely dissected by individual en-echelon faults, stretching from the Bodo Verde Fracture Zone in the north into the middle of the Cretaceous Magnetic Quiet Zone at its southeastern extension (Fig. 1b). This feature
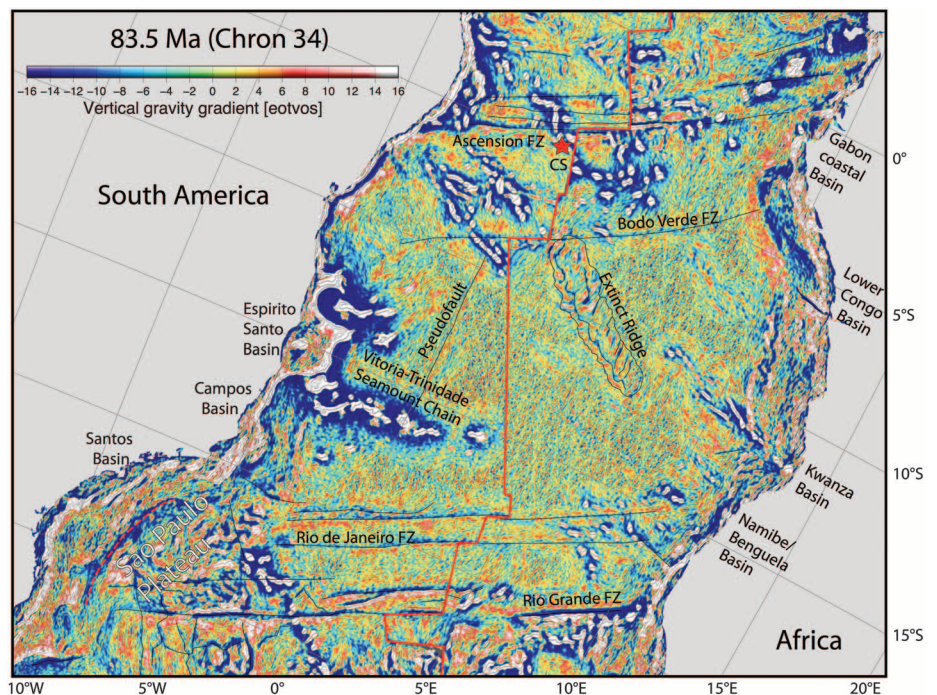
Fig. 3. South Atlantic filtered VGG. Reconstructed at chron 34 (83.5 Ma, orthographic projection) with Africa fixed (16). Major tectonic and volcanic sea-floor features and offshore sedimentary basins are labeled. The mid-ocean ridge is outlined in red, the extinct Abimael spreading ridge is shown as a dashed red line, and the reconstructed position of the Cardno hot spot (CS) is outlined by a red star. Most of the sea floor shown in this reconstruction was formed during the Cretaceous Normal Superchron. Also note that the extinct Abimael spreading ridge between the Santos Basin and Sao Paulo Plateau offshore of Brazil is now visible as a negative VGG anomaly (dashed red line), as compared to previous interpretations (17, 18). This region is of great interest for oil and gas exploration, as it is one of the most extensive deepwater oil and gas frontiers globally, with several recent discoveries (19).

is about 800 km long and 100 km wide and does not follow either the azimuth of nearby sea-floor isochrons or FZs. A reconstruction of this feature at magnetic chron 34 [83.5 million years ago (Ma)] (Fig. 3) reveals that it has a mirror-image counterpart on the South American plate, but this conjugate feature is represented only by a relatively faint gravity lineament (Fig. 3). This feature is visible in the filtered vertical gravity gradient image, marking a boundary between

swaths of differently textured sea-floor fabric to the east and west of the lineament (Fig. 3). The geometry of the two features suggests that they form a pair of an extinct ridge (on the African side) and a pseudofault (on the South American side), created by a northward ridge propagation episode between ~100 and 83 Ma. An absolute hot spot–based plate reconstruction using the rotation parameters from O'Neill *et al.* (*10*) indicates that the Cardno hot spot (Fig. 3) may have been situated not far north of the northern tip of the ridge propagator, where it abuts the Bodo Verde Fracture Zone; this is where the propagator came to a halt. These observations conform with the inference that ridges have a tendency to propagate toward hot spots/plumes and that propagation events and resulting spreading asymmetries are frequently contained within individual spreading corridors bounded by FZs (*11*). The existence of major previously unknown ridge propagation events will also be relevant for interpreting marine magnetic anomaly sequences during the Cretaceous Normal Superchron on conjugate ridge flanks (*12*).

One of the most important uses of this new marine gravity field will be to improve the estimates of sea-floor depth in the 80% of the oceans having no depth soundings. The most accurate method of mapping sea-floor depth uses a multibeam echosounder mounted on a large research vessel. However, even after 40 years of mapping by hundreds of ships, one finds that more than 50% of the ocean floor is more than 10 km away from a depth measurement. Between the soundings, the sea-floor depth is estimated from marine gravity measurements from satellite altimetry (*13*). This method works best on sea floor where sediments are thin, resulting in a high correlation between sea-floor topography and gravity anomalies in the 12-km–to–160-km wavelength band. The shorter wavelengths are attenuated because of Newton's inverse square law, whereas the longer wavelengths are partially cancelled by the gravity anomalies caused by the isostatic topography on the Moho (*13*). The abyssal hill fabric created during the sea-floor spreading process has characteristic wavelengths of 2 to 12 km, so it is now becoming visible in the vertical gravity gradient (VGG) models, especially on the flanks of the slower-spreading ridges (*14*). Additionally, seamounts between 1 and 2 km tall, which were not apparent in the older gravity models, are becoming visible in the new data. As CryoSat-2 continues to map the ocean surface topography, the noise in the global marine gravity field will decrease. Additional analysis of the existing data, combined with this steady decrease in noise, will enable dramatic improvements in our understanding of deep ocean tectonic processes.

REFERENCES AND NOTES

1. J. T. Wilson, *Nature* **207**, 343–347 (1965).
2. S. Cande, J. LaBrecque, W. Haxby, *J. Geophys. Res. Solid Earth* **93**, 13479–13492 (1988).
3. C. Heine, J. Zoethout, R. D. Müller, *Solid Earth* **4**, 215–253 (2013).
4. L. A. Lawver, L. M. Gahagan, I. W. Dalziel, *Mem. Natl. Inst. Polar Res.* **53**, 214–229 (1998).
5. M. S. Steckler, A. B. Watts, *Earth Planet. Sci. Lett.* **41**, 1–13 (1978).
6. C. S. Liu, D. T. Sandwell, J. R. Curray, *J. Geophys. Res.* **87**, 7673–7686 (1982).
7. K. Matthews, R. D. Müller, P. Wessel, J. M. Whittaker, *J. Geophys. Res. Solid Earth* **116**, 1–28 (2011).
8. Materials and methods are available as supplementary materials on *Science* Online.
9. J. Pindell, L. Kennen, in *The Geology and Evolution of the Region Between North and South America*, K. James, M. A. Lorente, J. Pindell, Eds. (Special Publication, Geological Society of London, London, 2009), vol. 328, pp. 1–55.
10. C. O'Neill, R. D. Müller, B. Steinberger, *Geochem. Geophys. Geosyst.* **6**, Q04003 (2005).
11. R. D. Müller, W. R. Roest, J. Y. Royer, *Nature* **396**, 455–459 (1998).
12. R. Granot, J. Dyment, Y. Gallet, *Nat. Geosci.* **5**, 220–223 (2012).
13. W. H. F. Smith, D. T. Sandwell, *Science* **277**, 1956–1962 (1997).
14. J. A. Goff, W. H. F. Smith, K. A. Marks, *Oceanography* **17**, 24–37 (2004).
15. N. K. Pavlis, S. A. Holmes, S. C. Kenyon, J. K. Factor, *J. Geophys. Res.* **117**, B04406 (2012).
16. M. Seton *et al.*, *Earth Sci. Rev.* **113**, 212–270 (2012).
17. W. Mohriak, M. Nóbrega, M. Odegard, B. Gomes, W. Dickson, *Petrol. Geosci.* **16**, 231–245 (2010).
18. I. Scotchman, G. Gilchrist, N. Kusznir, A. Roberts, R. Fletcher, in *The Breakup of the South Atlantic Ocean: Formation of Failed Spreading Axes and Blocks of Thinned Continental Crust in the Santos Basin, Brazil and Its Consequences For Petroleum System Development* (Petroleum Geology Conference Series, Geological Society of London, London, 2010), pp. 855–866.
19. W. U. Mohriak, P. Szatmari, S. Anjos, *Geol. Soc. London Spec. Publ.* **363**, 131–158 (2012).

NANOPHOTONICS

Chiral nanophotonic waveguide interface based on spin-orbit interaction of light

Jan Petersen, Jürgen Volz,* Arno Rauschenbeutel*

Controlling the flow of light with nanophotonic waveguides has the potential of transforming integrated information processing. Because of the strong transverse confinement of the guided photons, their internal spin and their orbital angular momentum get coupled. Using this spin-orbit interaction of light, we break the mirror symmetry of the scattering of light with a gold nanoparticle on the surface of a nanophotonic waveguide and realize a chiral waveguide coupler in which the handedness of the incident light determines the propagation direction in the waveguide. We control the directionality of the scattering process and can direct up to 94% of the incoupled light into a given direction. Our approach allows for the control and manipulation of light in optical waveguides and new designs of optical sensors.

The development of integrated electronic circuits laid the foundations for the information age, which fundamentally changed modern society. During the past decades, a transition from electronic to photonic information transfer took place, and nowadays, nanophotonic circuits and waveguides promise to partially replace their electronic counterparts and to enable radically new functionalities (*1*–*3*). The strong confinement of light provided by such waveguides leads to large intensity gradients on the wavelength scale. In this strongly nonparaxial regime, spin and orbital angular momentum of light are no longer independent physical quantities but are coupled (*4*, *5*). In particular, the spin depends on the position in the transverse plane and on the propagation direction of light in the waveguide—an effect referred to as spin-orbit interaction of light (SOI). This effect holds great promises for the investigation of a large range of physical phenomena such as the spin-Hall effect (*6*, *7*) and extraordinary momentum states (*8*) and has been observed for freely propagating light fields (*9*, *10*) in the case of total internal reflection (*11*, *12*), in plasmonic systems (*13*–*15*), and for radio frequency waves in metamaterials (*16*). Recently, it has been demonstrated in a cavity-quantum electrodynamics setup in which SOI fundamentally modifies the coupling between a single atom and the resonator field (*17*).

Vienna Center for Quantum Science and Technology, TU Wien–Atominstitut, Stadionallee 2, 1020 Vienna, Austria.
*Corresponding author. E-mail: jvolz@ati.ac.at (J.V.); arno.rauschenbeutel@ati.ac.at (A.R.)

New global marine gravity model from CryoSat-2 and Jason-1 reveals buried tectonic structure

David T. Sandwell *et al.*

Supplementary Materials for

New global marine gravity model from CryoSat-2 and Jason-1 reveals buried tectonic structure

David T. Sandwell,* R. Dietmar Müller, Walter H. F. Smith, Emmanuel Garcia, Richard Francis

*Corresponding author. E-mail: dsandwell@ucsd.edu

This PDF file includes:

Supplementary Text

<u>Gravity</u> <u>Anomaly</u> <u>Recovery</u>

Gravity anomalies are small differences in the pull of gravity associated with lateral variations in mass. The best approach to measuring marine gravity is to mount a very precise accelerometer on a ship. Unfortunately this ship coverage of the oceans is very sparse *(20)*. A second, now equally precise approach is to use an orbiting radar to measure the topography of the ocean surface, which is nearly an equipotential surface. The methods for recovering maps of marine gravity anomaly from radar altimeter data are discussed in many previous publications [e.g., *(21-24)*]. Some of the key technology developments related to this new marine gravity model are provided in two recent publications *(25, 26)*. For our investigation of crustal structure we use Laplace's equation to construct the first and second vertical derivatives of the potential called gravity anomaly and vertical gravity gradient, respectively. Images of these two fields over the South Atlantic Basin are shown in Fig. 1. The full resolution maps are best viewed using a computer display program such as Google Earth. The reader can download two small KMZ files to bring these full resolution maps into their computer. In addition they can download the gridded files to construct custom maps from http://topex.ucsd.edu/WWW_html/mar_grav.html .

<u>Improved</u> <u>Radar</u> <u>Technology</u>

The most important contribution of the new altimeters is related to a 1.25 times improvement in range precision *(26)*. This improvement is mainly related to an increase in the pulse repetition frequency (PRF) of the newer altimeters with respect to the older altimeters. The coherent nature of the radar signal results in speckle in the echoes, which masks the echo waveform and leads to imprecision in retrieval of its parameters. This can be alleviated by averaging successive echoes, but only up to the point that they become correlated, the onset of which has been generally assumed at a PRF of somewhat above 2 kHz at the common transmitter frequency of 13.5 GHz *(27)*. The newer altimeters CryoSat-2 and Jason-1 have PRFs of 1950 Hz and 2060 Hz, respectively while the older instruments were technologically limited to lower values of 1020 Hz. Theoretically this approximate doubling of PRF should result in a $\sqrt{2} = 1.41$ improvement in range precision; the actual improvement is somewhat smaller (1.25) perhaps reflecting the onset of echo correlation at the 2 kHz PRF. Nevertheless, this improvement in range precision maps directly into an improvement in gravity field accuracy.

CryoSat-2 was also operated in a new Synthetic Aperture Radar (SAR) mode over very limited areas of the oceans. This mode has a much higher PRF of 18.2 kHz and the highly correlated echoes are summed coherently in bursts of 64 pulses to form a long synthetic aperture. This enhances along-track resolution in the form of a set of narrow beams distributed in the along-track direction *(27–30)*. Unlike the conventional pulse-width limited geometry, the resulting echo waveforms have useful information in both the leading and trailing edges. This, together with an increase in the effective number of independent samples resulting from the SAR technique, reduces the height noise by a factor of ~1.4 compared to conventional LRM *(31)*. Comparison of height noise performance *(26)* indeed shows this expected improvement for CryoSat-2's SAR but similar gains for pulse-width limited echoes are obtained by a two-pass processing

scheme in which the slowly varying ocean wave-height is first estimated and smoothed and then excluded from the estimation process in the second pass. These results show that CryoSat-2's LRM performs slightly better than Jason-1 (which is already excellent), despite its reduced PRF. Much of the design of the two radars is common but it is likely that the improvements introduced for CryoSat-2's mission, particularly the higher transmitter power needed for operation over sloping ice surfaces and the extreme phase stability required for SAR interferometry, are contributing to this performance.

Coherence-Enhancing Filter

Despite the advances in satellite gravity anomaly image quality described in this paper, some high-frequency noise remains. In order to further improve the interpretation of linear tectonic features seen in the new vertical gravity gradient images, we have applied a filtering technique called coherence-enhancing diffusion to a selected region in the South Atlantic (Fig. 3) *(32)*. This filter combines anisotropic diffusion (a low-pass filter) with texture analysis, such that a diffusion tensor is computed from the local image structure so that the diffusion is parallel to linear features in the data. This type of filter has been successfully applied for enhancing noisy seismic reflection images to facilitate improved tracking of seismic horizons *(33)*, and is applied to vertical gravity gradient data here for the first time. While high-frequency noise has been suppressed, linear, coherent seafloor structures have been enhanced. In particular the internal en-echelon structure of the extinct mid-ocean ridge on the African Plate has been enhanced, while the juxtaposed differences in seafloor structure west and east of the conjugate pseudofault have been enhanced as well. Deeply buried linear structures of the Santos Basin and Sao Paulo Plateau offshore Brazil have been equally enhanced (Fig. 3), illustrating that improved satellite data combined with well-targeted filtering have a great potential to reveal previously hidden structures on abyssal plains and along passive margins.

Gravity Anomaly Uncertainty

We estimated the uncertainty in the gravity by calculating the rms difference in slope between individual altimeter profiles and the mean north and east slopes used to compute gravity (Fig S1.) The uncertainties were calibrated by comparisons with shipboard data from two completely different proprietary sources. First we computed the rms difference between the altimeter-derived gravity and more accurate shipboard gravity in a small region in the Gulf of Mexico. The ship data, provided by EDCON Inc., were collected on a very fine grid and have an rms crossover error of 0.5 mGal *(25)*. For this first comparison we found an rms difference of 1.60 mGal. In the second case, the altimeter-derived gravity data were compared with 30 million of the best shipboard data by the National Geospatial Intelligence Agency (NGA personal communication) resulting in an rms difference of 2.6 mGal. The rms difference is somewhat higher (3.6 mGal) in shallow areas (< 1 km) and somewhat lower (2.3 mGal) in deeper areas (3 - 6 km). On average, the NGA ship data have an rms error of 1 - 2 mGal. Assuming the mean rms error is 1.6 mGal then the mean rms error in the altimeter-derived gravity is ~2 mGal in agreement with the calibration derived from the Gulf of Mexico comparison. As shown in our previous study *(25)* most of the error reduction between this new gravity model and the older models occur in the 12 to 40 km wavelength band.

The noise reduction over the short wavelength band provides a dramatic improvement in the clarity of the vertical VGG signals. We used the Gulf of Mexico region to illustrate this noise reduction (Fig. S2). The upper plot shows the VGG derived from only Geosat and ERS-1 altimetry data *(24)* while the middle plot shows also includes the new measurements from CryoSat-2 and Jason-1. The reduction in noise between the old and new models reveals the extinct spreading ridges and transforms as well as the continent ocean boundary. One can also see some of these features in the old model but they are largely obscured by noise. The difference between the new and old model (Fig. S2 c) reveals the noise in the old model. The rms difference between the two models is 6.9 eotvos units and in terms of gravity anomaly (not shown) the rms difference is 2.2 mGal. The rms differences are zero over land, where the VGG and gravity anomaly are set by the EGM08 model *(9)*. Differences are greatest near the shorelines where the raw altimeter waveforms are sometimes contaminated by stray echoes off the land. To understand the contribution of each of the satellite data sets to the accuracy of the gravity grid, we have constructed a suite of gravity models after removing one of the non-repeat data sets. We find that because the four non-repeat altimeter data sets have differing orbital inclinations and noise levels they are all important for achieving the best overall accuracy.
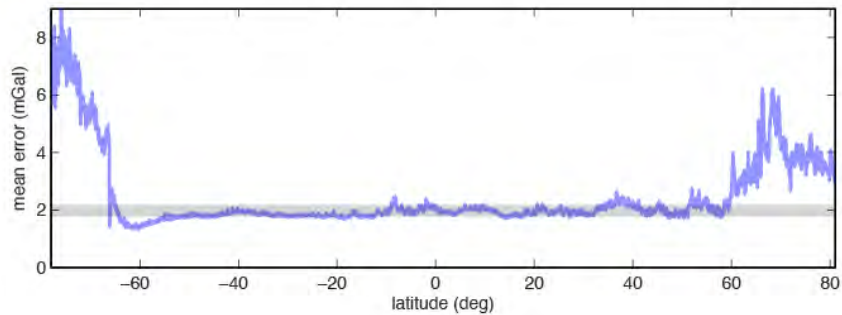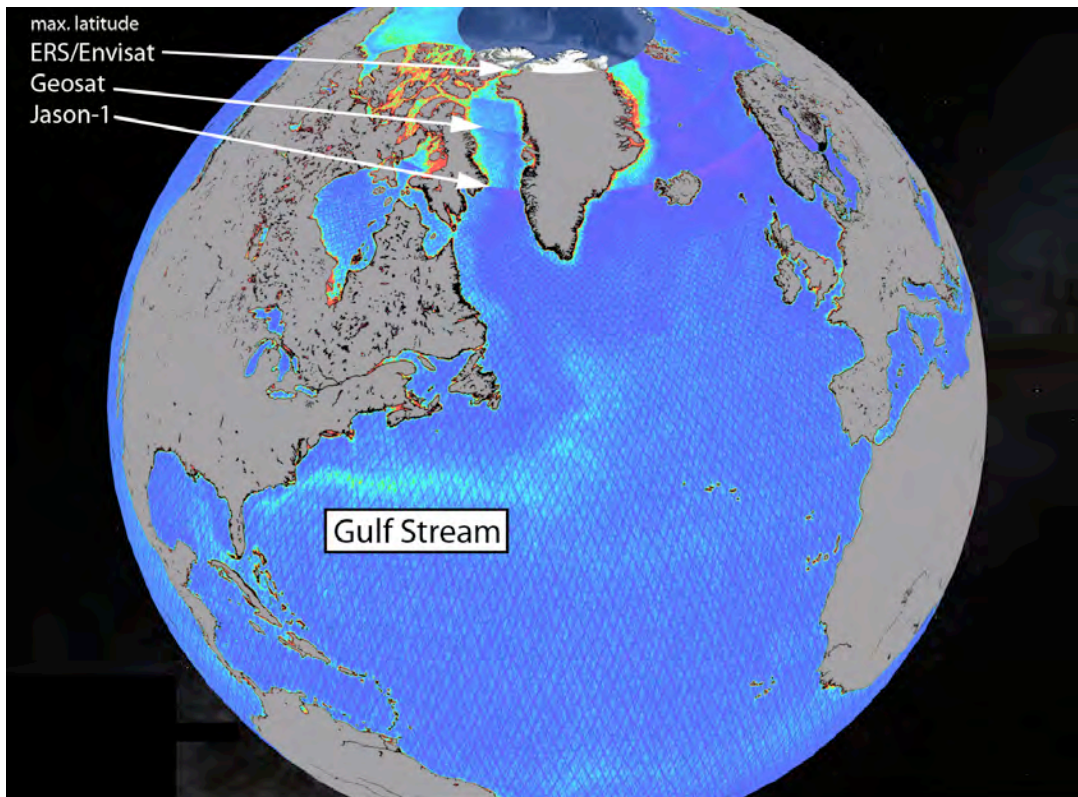
Fig. S1. Gravity error. (a) Estimated error in marine gravity anomaly to 81 degrees latitude. Color scale ranges from 0-10 mGal. Relatively larger noise occurs in areas of high mesoscale variability such as the Gulf Stream. Sharp changes in gravity noise occur at the maximum inclination of Jason-1, Geosat, ERS/Envisat ground tracks. (b) Longitude-averaged gravity error versus latitude. Noise is higher in polar regions due to lower track density and altimeter noise caused by sea ice. (Note CryoSat-2 collects data to 88 degrees latitude but this plot only extends to 81.)
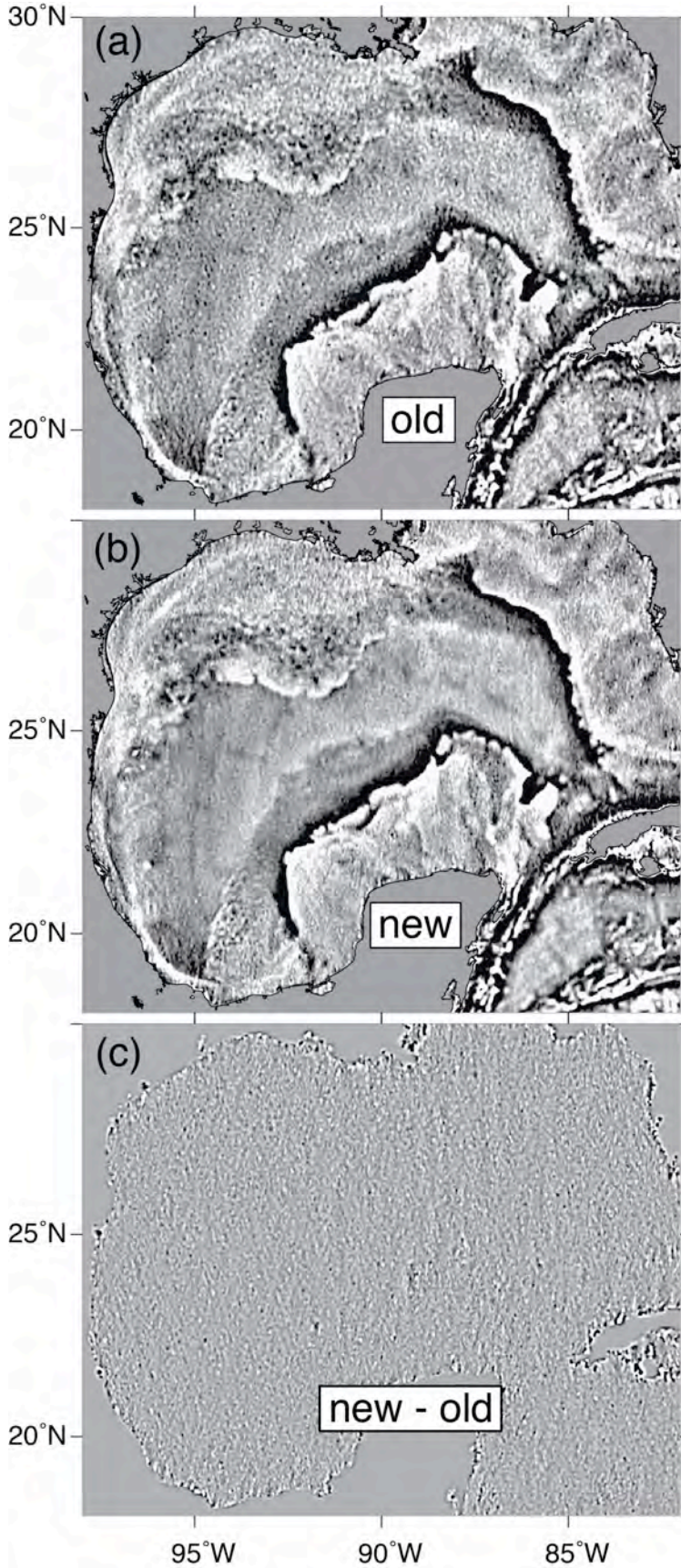
Fig. S2. Gulf of Mexico VGG. (a) Old VGG model based on Geosat and ERS-1. (b) New VGG model also includes data from CryoSat-2 and Jason-1. (c) Difference between the two models plotted using the same greyscale shows noise in the old VGG model. Mercator projection, grey scale saturates at +/- 20 eotvos units.

6

References and Notes

1. J. T. Wilson, A new class of faults and their bearing on continental drift. *Nature* **207**, 343–347 (1965). [doi:10.1038/207343a0](doi:10.1038/207343a0)

2. S. Cande, J. LaBrecque, W. Haxby, Plate kinematics of the South Atlantic: Chron C34 to present. *J. Geophys. Res. Solid Earth* **93**, 13479–13492 (1988). [doi:10.1029/JB093iB11p13479](doi:10.1029/JB093iB11p13479)

3. C. Heine, J. Zoethout, R. D. Müller, Kinematics of the South Atlantic rift. *Solid Earth* **4**, 215–253 (2013). [doi:10.5194/se-4-215-2013](doi:10.5194/se-4-215-2013)

4. L. A. Lawver, L. M. Gahagan, I. W. Dalziel, A tight fit—Early Mesozoic Gondwana, a plate reconstruction perspective. *Mem. Natl. Inst. Polar Res.* **53**, 214–229 (1998).

5. M. S. Steckler, A. B. Watts, Subsidence of the Atlantic-type continental margin off New York. *Earth Planet. Sci. Lett.* **41**, 1–13 (1978). [doi:10.1016/0012-821X(78)90036-5](doi:10.1016/0012-821X(78)90036-5)

6. C. S. Liu, D. T. Sandwell, J. R. Curray, The negative gravity field over the 85°E Ridge. *J. Geophys. Res.* **87**, 7673–7686 (1982). [doi:10.1029/JB087iB09p07673](doi:10.1029/JB087iB09p07673)

7. K. Matthews, R. D. Müller, P. Wessel, J. M. Whittaker, The tectonic fabric of the ocean basins. *J. Geophys. Res. Solid Earth* **116**, 1–28 (2011). [doi:10.1029/2011JB008413](doi:10.1029/2011JB008413)

8. Materials and methods are available as supplementary materials on *Science* Online.

9. J. Pindell, L. Kennen, in *The Geology and Evolution of the Region Between North and South America*, K. James, M. A. Lorente, J. Pindell, Eds. (Special Publication, Geological Society of London, London, 2009), vol. 328, pp. 1–55.

10. C. O'Neill, R. D. Müller, B. Steinberger, On the uncertainties in hot spot reconstructions and the significance of moving hot spot reference frames. *Geochem. Geophys. Geosyst.* **6**, Q04003 (2005). [doi:10.1029/2004GC000784](doi:10.1029/2004GC000784)

11. R. D. Müller, W. R. Roest, J. Y. Royer, Asymmetric sea-floor spreading caused by ridge-plume interactions. *Nature* **396**, 455–459 (1998). [doi:10.1038/24850](doi:10.1038/24850)

12. R. Granot, J. Dyment, Y. Gallet, Geomagnetic field variability during the Cretaceous Normal Superchron. *Nat. Geosci.* **5**, 220–223 (2012). doi:10.1038/ngeo1404

13. W. H. F. Smith, D. T. Sandwell, Global seafloor topography from satellite altimetry and ship depth soundings. *Science* **277**, 1956–1962 (1997). doi:10.1126/science.277.5334.1956

14. J. A. Goff, W. H. F. Smith, K. A. Marks, The contributions of abyssal hill morphology and noise to altimetric gravity fabric. *Oceanography* **17**, 24–37 (2004). doi:10.5670/oceanog.2004.64

15. N. K. Pavlis, S. A. Holmes, S. C. Kenyon, J. K. Factor, The development and evaluation of the Earth Gravitational Model 2008 (EGM2008). *J. Geophys. Res.* **117**, B04406 (2012). 10.1029/2011JB008916 [doi:10.1029/2011JB008916](doi:10.1029/2011JB008916)

16. M. Seton, R. D. Müller, S. Zahirovic, C. Gaina, T. Torsvik, G. Shephard, A. Talsma, M. Gurnis, M. Turner, S. Maus, M. Chandler, Global continental and ocean basin reconstructions since 200 Ma. *Earth Sci. Rev.* **113**, 212–270 (2012). doi:10.1016/j.earscirev.2012.03.002

17. W. Mohriak, M. Nóbrega, M. Odegard, B. Gomes, W. Dickson, Geological and geophysical interpretation of the Rio Grande Rise, south-eastern Brazilian margin: Extensional tectonics and rifting of continental and oceanic crusts. *Petrol. Geosci.* **16**, 231–245 (2010). doi:10.1144/1354-079309-910

18. I. Scotchman, G. Gilchrist, N. Kusznir, A. Roberts, R. Fletcher, in *The Breakup of the South Atlantic Ocean: Formation of Failed Spreading Axes and Blocks of Thinned Continental Crust in the Santos Basin, Brazil and Its Consequences For Petroleum System Development* (Petroleum Geology Conference Series, Geological Society of London, London, 2010), pp. 855–866.

19. W. U. Mohriak, P. Szatmari, S. Anjos, Salt: Geology and tectonics of selected Brazilian basins in their global context. *Geol. Soc. London Spec. Publ.* **363**, 131–158 (2012). doi:10.1144/SP363.7

20. M. T. Chandler, P. Wessel, Improving the quality of marine geophysical track line data: Along-track analysis. *J. Geophys. Res. Solid Earth* **113**, B02102 (2008). doi:10.1029/2007JB005051

21. O. B. Andersen, P. Knudsen, Global marine gravity field from the ERS-1 and Geosat geodetic mission altimetry. *J. Geophys. Res. Oceans* **103**, 8129–8137 (1998). doi:10.1029/97JC02198

22. W. Haxby, G. Karner, J. LaBrecque, J. Weissel, Digital images of combined oceanic and continental data sets and their use in tectonic studies. *EOS* **64**, 995–1004 (1983). doi:10.1029/EO064i052p00995

23. C. Hwang, B. Parsons, An optimal procedure for deriving marine gravity from multi-satellite altimetry. *Geophys. J. Int.* **125**, 705–718 (1996). doi:10.1111/j.1365-246X.1996.tb06018.x

24. D. T. Sandwell, W. H. F. Smith, Global marine gravity from retracked Geosat and ERS-1 altimetry: Ridge segmentation versus spreading rate. *J. Geophys. Res. Solid Earth* **114**, B01411 (2009). doi:10.1029/2008JB006008

25. D. Sandwell, E. Garcia, K. Soofi, P. Wessel, M. Chandler, W. H. F. Smith, Toward 1-mGal accuracy in global marine gravity from CryoSat-2, Envisat, and Jason-1. *Leading Edge* **32**, 892–899 (2013). doi:10.1190/tle32080892.1

26. E. S. Garcia, D. T. Sandwell, W. H. F. Smith, Retracking CryoSat-2, Envisat and Jason-1 radar altimetry waveforms for improved gravity field recovery. *Geophys. J. Int*. **196**, 1402–1422 (2014).

27. D. J. Wingham, C. R. Francis, S. Baker, C. Bouzinac, D. Brockley, R. Cullen, P. de Chateau-Thierry, S. W. Laxon, U. Mallow, C. Mavrocordatos, L. Phalippou, G. Ratier, L. Rey, F. Rostan, P. Viau, D. W. Wallis, CryoSat: A mission to determine the fluctuations in Earth's land and marine ice fields. *Adv. Space Res.* **37**, 841–871 (2006). doi:10.1016/j.asr.2005.07.027

28. H. D. Griffiths, Synthetic aperture processing for full-deramp radar altimeters. *Electron. Lett.* **24**, 371–373 (1988). [doi:10.1049/el:19880251](doi:10.1049/el:19880251)

29. W. T. K. Johnson, Magellan imaging radar mission to Venus. *Proc. IEEE* **79**, 777–790 (1991). [doi:10.1109/5.90157](doi:10.1109/5.90157)

30. R. K. Raney, The delay Doppler radar altimeter. *IEEE Trans. Geosci. Rem. Sens.* **36**, 1578–1588 (1998). [doi:10.1109/36.718861](doi:10.1109/36.718861)

31. L. Phalippou, V. Enjolras, Re-tracking of SAR altimeter ocean power waveforms and related accuracies of sea surface height, significant wave height, and wind speed. *Proc. IEEE IGARSS'07*, 3533–3536 (2007).

32. J. Weickert, Coherence-enhancing diffusion of colour images. *Image Vis. Comput.* **17**, 201–212 (1999). [doi:10.1016/S0262-8856(98)00102-4](doi:10.1016/S0262-8856(98)00102-4)

33. G. C. Fehmers, C. F. Höcker, Fast structural interpretation with structure-oriented filtering. *Geophysics* **68**, 1286–1293 (2003). [doi:10.1190/1.1598121](doi:10.1190/1.1598121)